Large-Scale Turbulence Structures and Their Contributions to the Momentum Flux and Turbulence in the Near-Neutral Atmospheric Boundary Layer Observed from a 213-m Tall Meteorological Tower

Mitsuaki Horiguchi · Taiichi Hayashi · Ahoro Adachi · Shigeru Onogi

M. Horiguchi · T. Hayashi

Disaster Prevention Research Institute,

Kyoto University, Gokanosho, Uji, Kyoto, Japan

Tel.: +81-774-38-4161

Fax.: +81-774-38-4158

e-mail: horiguchi@storm.dpri.kyoto-u.ac.jp

A. Adachi · S. Onogi

Meteorological Research Institute,

Japan Meteorological Agency, Tsukuba, Ibaraki, Japan

Abstract Large-scale turbulence structures in the near-neutral atmospheric boundary layer (ABL) are investigated on the basis of observations made from the 213-m tall meteorological tower at Tsukuba, Japan. Vertical profiles of wind speed and turbulent fluxes in the ABL were obtained with sonic anemometer-thermometers at six levels of the tower. From the archived data, 31 near-neutral cases are selected for the analysis of turbulence structures. For the typical case, event detection by the integral wavelet transform with a large time scale (180 s) from the streamwise velocity component (u) at the highest level (200 m) reveals a descending high-speed structure with a time scale of approximately 100 s (a spatial scale of 1 km at the 200-m height). By applying the wavelet transform to the u velocity component at each level, the intermittent appearance of large-scale high-speed structures extending also in the vertical is detected. These structures usually make a large contribution to the downward momentum transfer and induce the enhancement of turbulent kinetic energy. This behaviour is like that of “active” turbulent motions. From the analysis of the two-point space-time correlation of wavelet coefficients for the u velocity component, the vertical extent and the downward influence of large-scale structures are examined. Large fluctuations in the large-scale range (wavelet variance at the selected time scale) at the 200-m level tend to induce the large correlation between the higher and lower levels.

Keywords *Atmospheric boundary layer · Coherent structures · Momentum transfer · Turbulent kinetic energy · Wavelet transform*

1 Introduction

Coherent structures are intermittent and spatially local flow patterns in turbulence, which have been identified in many types of flow, such as boundary-layer flow (e.g. Kline et al.

1967) and pipe flow (e.g. Corino and Brodkey 1969). Many laboratory experiments have demonstrated the existence of coherent turbulence structures and their large contributions to turbulence and turbulent transfer. These experiments were mostly performed under conditions of low Reynolds number ($Re < 10^4$), but in the case of the atmospheric boundary layer (ABL), conditions are very different, because the Reynolds number of the flow is very high ($Re \approx 10^8$).

Turbulence structures in the ABL have previously been investigated using large-eddy simulation (LES) models and various measurement techniques in field experiments. LES models, in which large eddies are resolved and subgrid-scale turbulence is parametrized, are capable of handling high Reynolds number flow. Many studies on turbulence structures in the ABL have been performed using LES (e.g. Deardorff 1972; Lin et al. 1996).

Small-scale structures known as microfronts (Gao et al. 1989, 1992; Mahrt and Howell 1994) or gust fronts (Hayashi 1992) have been found in field experiments investigating turbulence in the surface layer. Microfrontal structures were observed also from low-level aircraft flights (Mahrt 1991), such structures containing distinct high-speed regions, representing certain types of coherent structures in the ABL. Since these experiments were conducted only in the region near the surface, the vertical extent of the structures in the ABL is unclear. The development of remote sensing using e.g. a Doppler lidar made it possible to visualize three-dimensional flow patterns in the ABL. Drobinski et al. (2004) showed the structures elongated in the streamwise direction close to the ground with organized regions of high-speed and low-speed fluid (streaks). Many types of coherent structures have been observed in the ABL, and these structures exist under a variety of atmospheric stability conditions (Lu and Fitzjarrald 1994; Barthlott et al. 2007). Nevertheless, turbulence structures at higher levels in the ABL have not been investigated in detail from observations.

From theoretical considerations and experimental data, Hunt and Morrison (2000) suggested that the dominant mechanism for the neutrally stratified turbulent boundary

layer at very high Reynolds numbers is the impingement of “large-scale eddies” at the wall and the subsequent generation of shear stresses within internal shear layers. This “top-down” picture differs from the “bottom-up” instability–surface interaction mechanisms proposed in most previous studies. Subsequently, Hunt and Carlotti (2001) studied the essential mechanisms for turbulent eddies impinging on the wall by using linearized rapid distortion theory. Drobinski et al. (2007) presented evidence of the multiscale nature of turbulent eddies in the neutral surface layer from the combined use of an experimental database and numerical simulations. This evidence is consistent with the top-down picture in Hunt and Morrison (2000).

Townsend (1961) supposed that the turbulent motion in a layer with equilibrium between energy production and dissipation consists of an “active” component responsible for turbulent transfer and an “inactive” component that is not involved in the transfer. This hypothesis was supported by Bradshaw (1967) using frequency spectra in a strongly retarded boundary layer, in which the large-scale “inactive” motion arising in the outer layer is particularly intense. Recently, the various atmospheric neutral surface-layer characteristics identified as the effects of the “inactive” turbulence were explained by Högström et al. (2002) in terms of the “top-down” mechanism. They indicated that “detached eddies” of relatively large scale, which are brought down from above into the surface layer, cause the increase of dimensionless vertical velocity variance with height as well as other anomalies. In contrast to the previous studies, these eddies, features of which are similar to the “inactive” turbulence, are a very effective means for momentum transport.

As in the above investigations, it is important to examine the momentum transfer process in the lower part of the boundary layer, particularly the intrusion of fast-moving upper regions upon the surface. As an example, Zeng et al. (2010) revealed gust-wind wave packets with a period of 3–6 min following the passage of a cold front. They also showed that the gust wind characterized by a coherent structure is very favourable for soil erosion and sand/dust emission, and can induce the further entrainment of dust particles

into the middle and upper levels of the ABL.

The purpose of the present study is to investigate the features of coherent turbulence structures in the neutral ABL and their effects on related processes, such as momentum transfer and the intensity of turbulence. The neutral boundary layer is defined here for conditions in which the mechanical (shear) production of turbulent kinetic energy (TKE) is much larger than the buoyant production. Turbulence structures in such a neutral boundary layer with small buoyancy effects are expected to have different geometric aspects from those in the stable or unstable boundary layer. In the near-neutral ABL, Horiguchi et al. (2010) revealed a descending large-scale high-speed structure using a Doppler sodar and sonic anemometer. Although this structure was of large extent in the vertical direction, precise measurements by the sonic anemometer were limited to the surface layer. The present study is intended to investigate the characteristic features of large-scale high-speed structures up to levels above the surface layer, and their effects on the momentum transfer and the intensity of turbulence. We use observations from a meteorological tower, so that time variations of wind speed in the lower part of the ABL, up to a sufficiently high level, are analyzed.

2 Observations

2.1 Outline of Observations

For observational studies of the ABL, the 213-m tall meteorological tower was constructed at the Meteorological Research Institute (MRI), Japan Meteorological Agency in 1975. The MRI is situated in Tsukuba City, which is located in a suburb of Tokyo and on the Kanto Plain of Honshu Island (main island), Japan (36.1°N, 140.1°E). The surface of the plain is roughly flat; even so, this observational site is sparsely surrounded by trees and buildings (typical height of 20–30 m for tall ones) over a large area. The meteorological tower has a guyed open lattice structure and a triangular cross-

section with 4-m sides.

On the tower, sonic anemometer-thermometers (DAT-300, Kaijo Co., Tokyo, Japan) were installed at levels of 10, 25, 50, 100, 150, and 200 m for the measurement of the fluctuations in the three velocity components and temperature. The sampling rate for this instrument was 10 Hz. At each level, three booms (towards approximately the north-west and north-east, and exactly the south directions) of 6-m length were stretched from the tower and a sonic anemometer-thermometer was set on each boom. Instruments on the windward side were selected and the data from them were stored, depending upon the wind direction, measured by a sonic anemometer at the top (213 m) of the tower. In addition to the turbulence observations, standard meteorological elements were measured at each level using propeller anemometers with wind vanes, resistance thermometers, and capacitance hygrometers. Many investigations have been carried out, including the analysis of turbulence characteristics (Hanafusa and Fujitani 1981).

Data analysis in this study is executed for the observational cases, in which thermal conditions in the boundary layer were near neutral. Here, we use the surface-layer scaling parameter (ζ), the ratio of the height z to the scaling length L (the Obukhov length), where

$$\zeta = z / L = -\frac{\left(g / \overline{T}\right)\left(\overline{w'T'}\right)_0}{u_*^{\,3} / kz}, \tag{1}$$

and g is the acceleration due to gravity, T is the absolute temperature, w is the vertical velocity component (positive upward), u_* is the friction velocity, and k is the von Karman constant (= 0.4). The overbar denotes the time average, the prime denotes the fluctuation from the mean (averaged value), and $(\,)_0$ is the surface value. The friction velocity (u_*) is given by

$$u_* = \left(\tau_0 / \rho\right)^{1/2} = \left[-\left(\overline{u'w'}\right)_0\right]^{1/2}, \tag{2}$$

where τ_0 is the surface shear stress, ρ is the density of air, and u is the streamwise velocity component (the velocity component in the direction of the mean wind vector). Here, $-\rho\overline{u'w'}$ is the vertical (downward) eddy flux of streamwise momentum and is referred to as the Reynolds shear stress. In this study, the direction of the mean flow is decided from the original data every 30 min and the eddy flux is calculated over this averaging time. In Eq. 1, fluctuating components are obtained by the sonic anemometer-thermometers and $\overline{T}$ is obtained from the resistance thermometers.

For conditions not far from neutral stability, the parameter ζ (= z/L) has essentially the same meaning as the flux Richardson number (R_f), which is the ratio of the buoyant production of turbulence to its shear production. Specifically, conditions in the range $|z/L| < 0.2$ at the 50-m level ("base level") in the surface layer are considered to be near-neutral in this study. This higher level (50 m) has been selected owing to the more vigorous turbulence at the 25-m level, which is caused by the surrounding roughness elements (trees etc.). The lower levels, which are more strongly disturbed than the higher levels, are not dealt with in the detailed discussion of the observational results.

In our analysis, usually the u velocity component at all levels is taken in the horizontal plane at each height and in the same horizontal direction as the mean wind at the 50-m level. Applying Taylor's frozen turbulence hypothesis, this procedure makes it possible to interpret the change of the wind profile (u) in one vertical section. In this coordinate system, the w velocity component is taken in the direction of the upward normal to the u velocity component (in the vertical direction). However, to be precise, the three-dimensional mean wind vector may not be situated in the horizontal plane. Therefore, for the analysis of the eddy flux that is sensitive to the choice of the reference frame, a coordinate transformation is applied. First, the three-dimensional mean wind direction is decided from the original three velocity components in the instrument's reference frame. Next, the u component is taken in the three-dimensional mean wind direction, and the w component is taken in the direction of the upward normal to this mean wind direction. In the rotated frames, the u component at each level is not

necessarily directed towards the same direction on the horizontal plane.

2.2 Cases for the Analysis

For the survey of the whole set of data, daily files are divided into 30-min data segments (parts), while the analysis of time-averaged statistics applies to individual parts. One observational case is a series of measurements during 210 min (seven parts), in which near-neutral conditions apply. This period is chosen to identify a sufficient number of large-scale turbulence structures and to prevent the significant change of conditions during a case. We did not discard the cases in which some change of wind condition was observed. If near-neutral conditions continue longer than 210 min, the period of the smallest average $|z/L|$ is selected.

For the observations during the period from December 1999 to March 2000 (a cold and windy period) near-neutral cases ($|z/L| < 0.2$ at the 50-m level) were selected. The cases with extremely weak turbulence at the top level (200 m), in which the turbulence intensity (the ratio of the standard deviation of the u velocity component to the mean u, $\sigma_u / \overline{u}$) is less than 0.05, are not used for the analysis. Higher levels in such cases are likely to be situated in the elevated stable layer and separated from the lower levels. With no availability of special sensors, the vertical structure throughout the ABL was unknown during the observations. In addition, any case in which a large deviation of wind direction (larger than 20°) from that of the 50-m level was observed at any level is also not used for the analysis.

The mean conditions of wind direction, horizontal wind speed, friction velocity (u_*), and the magnitude of the surface-layer scaling parameter ($|z/L|$), all of which are evaluated at the 50-m level, are listed in Table 1. In total, 31 cases were selected and observations are referred to as case No. 1–31. The weather on the days for these cases was reported by the Japan Meteorological Agency as fair in most cases (27 cases) or cloudy in the other cases at 0900 or 1500 local standard time (LST) at the nearby Tateno

station in Tsukuba City. In the case of wind directions in the range of approximately west-south-west to north, the data at the 150-m level were not acquired owing to some problem of the instrument on a boom in the north-west direction.

Mean wind speeds ranging from 4.9 to 11.1 m s^{-1} and mean friction velocities (u_*) from 0.5 to 1.12 m s^{-1} indicate no large variation of wind conditions among the cases. Assuming the logarithmic wind profile under neutral conditions, the roughness length z_0 was calculated in the range of 0.6–2.4 m from the mean u (50-m level) and the friction velocity u_*. Compared with the typical values for natural surfaces (e.g. Garratt 1992), z_0 has slightly larger values owing to the trees and buildings surrounding the tower.

3 Results and Discussion

3.1 Large-Scale High-Speed Structures in the Observational Cases

In this section, first of all we examine a typical case. We selected the case from 1330 to 1700 LST on March 29, 2000 (case No. 29) based on the following criteria: (1) data were acquired at every measurement level on the tower; (2) this case shows the lowest average $|z/L|$ among the cases in the daytime and afternoon. The majority of cases (20 cases) were observed for this period of the day (the starting time is in the range of 1230–1600). In case No. 29, the weather was cloudy at 1500 LST and the average horizontal wind speed is 8.6 m s^{-1} at the 50-m level. The mean wind speed in each part changes from 10.3 (part 1) to 6.1 m s^{-1} (part 7) over a period of one observational case. The wind direction is mainly south-south-west (195–207°).

We inspected the time series of the u velocity component at each level for case No. 29. As is explained in Sect. 2.1, the u component at all levels is taken in the same direction as the mean wind at the 50-m level. In this case, the deviation of the mean wind direction at each level is not large (less than 8.6° in each part), and on average the wind speed (u)

varies logarithmically with height up to the level of 150 m. The average value of u reaches 12.2 m s^{-1} at the highest level (200 m). The time series of the u component shows wind fluctuations due to a superposition of turbulent eddies with a wide range of time scales. Superimposed on the small-scale fluctuations, the regions of high speed with a roughly estimated time scale of 100–200 s are seen. These large-scale regions are extensive also in the vertical direction. For the same period of the case, the w velocity component at each level shows comparatively small-scale fluctuations. Temporal variations corresponding to those in the u component are sometimes discernable.

The extent of the regions of high speed is readily recognized in the time–height cross-section of the u velocity component (Fig. 1, for part 1). Before depicting the contours, block averaging every 20 data points (during 2 s) was applied to diminish the fine-scale variations. This figure demonstrates the vertical coherence of high-speed events. In fact, large-scale regions of high speed (e.g. the area of $u > 14$ m s^{-1}) at the higher levels (200 and 150 m) extend down to the lower level (25 m).

For the first stage of the analysis, spectral characteristics of turbulence at each level are examined. Here, velocity components are taken with reference to the three-dimensional mean wind direction in the manner described in Sect. 2.1. Frequency (f)-weighted power spectra for the u and w components (P_u and P_w) for each part are normalized with respect to u_*^2 (at 50 m) and represented as a function of the non-dimensional frequency n ($= fz/\overline{u}$). Further, these spectra are averaged over parts 1 to 7 and smoothed with a frequency window after Kaimal and Finnigan (1994). This frequency window expands in width with frequency to reduce the large scatter of spectral estimates in the higher frequency. For the spectra in Fig. 2, broad peaks are observed in the non-dimensional frequency range of approximately 0.01–0.2 for the u component. By contrast, spectra for the w component have narrow peaks of approximately 0.2–0.8 (not shown here). Represented on a scale of non-dimensional frequency, these spectra undergo a small variation with height.

As the non-dimensional frequency n is the ratio of height z to wavelength λ ($= \overline{u}/f$),

the peak location of the spectrum at each level corresponds to the larger spatial scale (λ) at the higher levels and the smaller spatial scale at the lower levels. For the *u* velocity component, spectral peaks lie in the range of approximately 1,000–20,000 m on a spatial scale at the 200-m level and 600–3,000 m at the 50-m level. For the *w* velocity component, peaks are located at the spatial scale of approximately 500 m at the 200-m level and 100–200 m at the 50-m level.

These features are almost similar to the results in previous studies for the surface-layer spectra under neutral stability (e.g. Kaimal and Finnigan 1994). Moreover, broad spectral peaks recognizable in the spectra for the *u* velocity component are likely to correspond with the region of the –1 power law in which P_u decays as κ_1^{-1} (κ_1 is the streamwise wavenumber). This region revealing turbulence anisotropy in the surface layer has been indicated previously through experiments (e.g. Davenport 1961) and theoretical studies (e.g. Hunt and Carlotti 2001).

Turbulence structures of various scales are extracted by applying an integral wavelet transform to the time series of data $x(t)$. The wavelet transform (wavelet coefficient) $T_p(a, b)$ with a scale parameter a and a translation parameter b is defined as

$$T_p(a,b) = \left(\frac{1}{a}\right)\int_{-\infty}^{+\infty} \Psi\left(\frac{t-b}{a}\right)^{*} x(t)\,dt\,, \tag{3}$$

where the function $(1/a)\Psi((t-b)/a)$ is a wavelet, and $\Psi(t)$ is called the analyzing wavelet (mother wavelet). The asterisk denotes the complex conjugate of the function. The scale parameter a alters the length and amplitude of the wavelet, and the translation parameter b sets the location of the wavelet in time. The wavelet transform detects only the local variation of data series, and the discrete form of Eq. 3 is applied to the present data.

For the analyzing wavelet, the “Mexican Hat” wavelet function is employed as in other studies on turbulence (e.g. Gao and Li 1993; Chen and Hu 2003), given by

$$\Psi(t) = (1 - t^2) \exp(-t^2/2). \quad (4)$$

This function is well localized in both time and frequency, and it has a smooth and symmetrical shape. The scale parameter a is the half-width of the positive part of this wavelet function and the time scale defined by the value of $2a$ is used for sorting structures according to their scale. Additionally, in order to examine the representative scale of structures, the wavelet variance spectrum $W(a)$ (Mahrt 1991; Collineau and Brunet 1993; Thomas and Foken 2007) is calculated as follows:

$$W(a) = \int_{-\infty}^{+\infty} \left| T_p(a, b) \right|^2 db. \quad (5)$$

The integral wavelet transform is applied to the data series of the streamwise velocity component in the horizontal plane (u), which is measured by the sonic anemometer at each level. Fluctuations normalized with respect to the standard deviation (σ_u) in each part are used for this analysis. Moreover, block averaging every 20 data points (for 2 s) is applied to diminish the fine-scale variations, and the resulting data are connected over seven parts. For the averaged data, the smallest time scale ($2a$) for the wavelet transform is 4 s. Figure 3 shows the wavelet variance spectra for the u component of case No. 29 at all levels as a function of the time scale, and which indicate that global maxima are located in the large-scale range (> 100 s) at the higher levels (100–200 m). These broad spectral maxima are partly due to the spectral redundancy of the wavelet variance using the Mexican Hat function. Positions of these maxima correspond to the time scales of 144 s at the 100-m, 172 s at the 150-m, and 180 s at the 200-m level.

Wavelet variance spectra for the u velocity component can be depicted as a function of the reciprocal of the non-dimensional time scale ($(2a\bar{u}/z)^{-1}$) (not shown here) for the comparison with the power spectra using the Fourier transform (a function of non-dimensional frequency). Here, it should be noted that the time scale ($2a$) of the wavelet

transform and the period (1/*f*) of the Fourier transform is defined individually for each transform. In contrast to the power spectra (Fig. 2), the wavelet variance spectra in both representations indicate clear maxima at the higher levels. This difference probably derives from the high spectral resolution of the wavelet variance spectrum in the low frequency range (large time scale). Although the wavelet variance cannot distinguish the contributions by the high-speed and low-speed structures in principle, these maxima can be attributed to the large-scale regions of high speed, which are shown in Fig. 1. These large-scale regions are specifically examined in the following analysis. When time scales are converted into spatial scales using Taylor's frozen turbulence hypothesis, the time scale of 180 s at the 200-m level corresponds to a scale of approximately 2,200 m from the mean wind speed at this level.

Clear maxima of wavelet variance spectra in the large-scale range at the higher levels are not always found in the other observational cases. In 17 cases (including case No. 29), the wavelet variance spectra for the *u* velocity component at the 200-m level exhibit a global or local maximum within the time scale range of 100–300 s. This range is prescribed for "large-scale" structures in this analysis. Figure 4 shows the wavelet variance spectra of an example case from 0000 to 0330 LST on March 29 2000 (case No. 27), in which a global maximum of the spectrum for the *u* component at the 200-m level is located at a time scale of 24 s. Likewise, in the cases during nighttime (four cases in total), a maximum is not found within the time scale range of 100–300 s (large-scale range). The power spectra for this case (case No. 27) do not indicate the region of the –1 power law (not shown), which is not identical to those in case No. 29. As in the above cases, the power spectra give comparable results with the wavelet variance spectra also in the other observational cases.

Since a descending high-speed structure with a large scale has been revealed in Horiguchi et al. (2010), the representative time scale of 180 s obtained at the highest level (200 m) is used for detecting large-scale high-speed structures, which are likely to have a downward movement from the even higher level. From the series of wavelet coefficients

on the translation parameter *b*, which is calculated from the *u* velocity component at the 200-m level, we select typical high-speed events with local maxima exceeding a threshold value. This threshold value has an effect on the number of the detected events and the resulting averaged pattern of the structure. In order to capture a distinctive and representative structure with a sufficient number of events, a certain threshold value is applied (1.3 to this case from visual inspection). Specifically, this value for detecting the typical events is higher than that (0.5) used for extracting the regions of high-speed structures in the subsequent part of this study. Using the data measured at each level, a conditionally-averaged pattern is then constructed from six detected events in this case and depicted on a time–height cross-section (zero corresponds to the time of the events) (Fig. 5). The fluctuations of the *u* and *w* velocity components, normalized with respect to their standard deviations (σ_u and σ_w) and averaged every 20 data points, are used for the averaging procedure. In Fig. 5, normalized u' values are indicated by the contours, and normalized w' values are denoted by the arrows. In addition, time progresses in the direction from the right to the left.

A descending high-speed structure with an estimated time scale of approximately 100 s is recognized from the averaged flow pattern of Fig. 5. The maximum value of u'/σ_u reaches 1.8 at 100-m height, while the average values of $\overline{u}$ and σ_u over parts 1 to 7 are 10.8 and 1.9 m s^{-1} at that height. On the other hand, the maximum value of w'/σ_w is −1.1 at 150-m height (average σ_w is 1.2 m s^{-1}). The upper portion of this high-speed structure appears a little earlier than its lower portion. Therefore, when the temporal variation is converted into the spatial distribution, this pattern shows a high-speed structure tilting towards the downwind direction, the scale of which is approximately 1 km from the mean wind speed at the 200-m level. In advance of the high-speed structure, a low-speed region ascending slightly at the time of approximately 100 s prior to the events is also revealed. The high-speed structure has a large scale in the streamwise direction and appears to be the same type as that presented in Horiguchi et al. (2010). In their study, the scale of the structure was estimated to be 400–800 m.

The detection of large-scale high-speed structures and the construction of the averaged flow pattern are also made for all other observational cases. For the wavelet transform, the time scale at which the wavelet variance spectrum for the *u* velocity component at the 200-m level indicates a global or local maximum in the range of 100–300 s is used. When a maximum is not identified in this range, the time scale corresponding to the spatial scale for case No. 29 is selected based on the mean wind speed at the 200-m level. As a result of the analysis, all patterns show similar descending high-speed structures.

In order to extract the large-scale structures on a time–height cross-section, the integral wavelet transform with the same time scale is applied for the *u* velocity component at each level. Figure 6 is a time–height cross-section of wavelet coefficients with the time scale of 180 s for case No. 29. The areas of warm colours in the time–height cross-section, corresponding to the high-speed structures, appear intermittently and extend widely in the vertical.

The regions of high-speed structures in the time–height cross-section are delineated with a threshold value for wavelet coefficients. Changing the threshold value alters the number and duration of high-speed structures. From the examination of this case, the definitive selection of the threshold value was difficult, and so a threshold value of 0.5 introduced in Horiguchi et al. (2010) is employed herein for the comparison of results. Accordingly, 25 periods of high-speed structures during the full observation time (198 min for the analysis) are detected from the wavelet coefficients for the *u* velocity component at the 200-m level. Since the threshold value (1.3) used for depicting the averaged flow pattern is higher than that (0.5) in this analysis, the previously detected high-speed events are included in these high-speed structures. The mean duration of the structures is 130 s and their time fraction of the total period is 27%. Furthermore, from the total number of structures, the mean interval of time between the structures is 480 s, corresponding to a spatial scale of 5,800 m.

For the analysis of the other observational cases, the time scale decided above is used

for the wavelet transform. Furthermore, the same threshold value (0.5) for wavelet coefficients as in case No. 29 is used. For these cases (including case No. 29), the mean duration of the structures is in the range of 72–200 s. In the same way, the mean interval of time between the structures lies in the range of 310–890 s, which corresponds to the spatial scale in the range of 3,100–8,300 m. In spite of the difference in the detection level (40 or 75 m in the previous study), the mean distance between the high-speed structures is similar to that of 3,800–5,400 m evaluated in Horiguchi et al. (2010).

3.2 Contributions of High-Speed Structures

Possible contributions of large-scale high-speed structures to turbulent transfer and TKE are examined in this section. First, in order to evaluate the relative importance to momentum transfer, the average value of instantaneous $u'w'$ in the large-scale high-speed structures decided above is compared with the overall average value of $u'w'$ for the entire analyzed period. This ratio is the same as the transport efficiency of structures (Barthlott et al. 2007). For the $u'w'$ value, the u and w velocity components are taken in the reference frame based on the three-dimensional mean wind vector. A negative value of $u'w'$ implies a downward transfer of momentum. For the case of 1330–1700 LST on March 29, 2000 (case No. 29), the magnitudes of the average $u'w'$ values in the structures are larger than those of the overall averages, the ratios of which are in the range 1.1–1.54 for the levels of measurements (Fig. 7). A maximum of $u'w'$ at the 25-m level is attributable to the more vigorous turbulence at this level. Accordingly, large-scale high-speed structures make a large contribution to momentum transfer throughout the layer from the near-surface to the higher level.

Turbulent motions are classified into four quadrants on the u', w' plane: (1) $u' \geq 0$, $w' \geq 0$ (outward interaction), (2) $u' < 0$, $w' \geq 0$ (ejection), (3) $u' < 0$, $w' < 0$ (inward interaction), and (4) $u' \geq 0$, $w' < 0$ (sweep) (Wallace et al. 1972; Willmarth and Lu 1972). In these quadrants, ejection and sweep motions contribute to the downward transfer of

momentum ($u'w' < 0$). The ejection motion is a low-speed upward turbulent motion and the sweep motion is a high-speed downward turbulent motion. Here, the flux fraction, which is a relative contribution of the motion in each quadrant to the downward momentum flux ($-\rho\overline{u'w'}$) by all motions, is examined for the entire period and only in the large-scale high-speed structures. Moreover, for the comparison of fluxes between the levels, $-\overline{u'w'}$ due to all motions at the 50-m level is used as a reference value at all levels. These normalized flux fractions are shown in Fig. 8 for case No. 29. For the entire period of case No. 29, the flux fraction due to ejection motions is slightly (21–42%) larger than that due to sweep motions for the 50-m level and above. For the lower levels, the contribution of sweep motions becomes nearly equal (25 m) or large (10 m) relative to that of ejection motions. This behaviour is almost consistent with the previous observational results (e.g. Drobinski et a1. 2004). Moreover, the same tendency is recognizable in the other cases, except for those observed during nighttime. Even though near-neutral conditions are the same for all observations, a different feature of the turbulent motion, that is, a large contribution of sweep motions at the higher level, is found during nighttime.

In contrast, in the large-scale high-speed structures, the flux fraction due to sweep motions is larger than that due to ejection motions at all levels. Since high-speed structures have relatively large values of the u velocity component, this may be a straightforward result. As regards the sweep motion, accumulated $u'w'$ values for this motion at the 200 and 50-m levels in the high-speed structures (time fractions of 27 and 26%) amount to 61 and 55% of the momentum flux carried by the sweep motion during the entire period.

Large-scale high-speed structures have a significant effect on the downward momentum transfer and the sweep motion, which implies their downward movements as a whole. Indeed, the downward vertical velocity averaged in the structures reaches 0.1–0.4 m s^{-1} at each level. Furthermore, the maximum downward velocity is found at the highest level (200 m).

Next, contributions of large-scale high-speed structures to the TKE are examined. TKE is evaluated as follows:

$$\bar{e} = (\overline{u'^2 + v'^2 + w'^2})/2, \tag{6}$$

where v is the lateral velocity component. For this analysis, three velocity components are also taken with reference to the three-dimensional mean wind vector. In the same manner as that for the value of $u'w'$, the average value of the instantaneous e (= $(u'^2+v'^2+w'^2)/2$) in the large-scale high-speed structures is compared with the overall average value (TKE) for the entire analyzed period in case No. 29 (Fig. 9). A maximum of TKE at the 25-m level is also attributable to the more vigorous turbulence at this level. The average e in the structures is nearly equal to or larger than the overall average, the ratio of which (enhancement factor) increases from 0.99 at the 200-m to 1.39 at the lowest level (10 m). This analysis reveals the more vigorous turbulence (large TKE) in the large-scale high-speed structures and the larger influence of the structures in the lower levels.

The same analyses of the contributions of large-scale high-speed structures for the momentum transfer and turbulence (TKE) are also made for the other observational cases. For all cases (including case No. 29), mean vertical profiles of the transport efficiency (ratio of the $u'w'$ value) and enhancement factor of TKE by the large-scale high-speed structures are shown in Fig. 10. Horizontal bars denote the standard deviations from the mean values. Owing to the problem of the instrument, only a small number of cases (five cases) could be used for the 150-m level. The mean values of the transport efficiency are > 1, with larger efficiencies occurring at lower levels. For example, at the 50-m level (base level for the analysis), transport efficiencies are > 1 in most cases (25 cases). Generally, large-scale high-speed structures make a large contribution to momentum transfer from the lower level (in the surface layer) to the higher level. For the value of TKE, enhancement factors at the 200-m level are not large, having a mean value of 1.01. This mean value increases at the lower levels, and the enhancement factors are > 1 in

most cases at the 50-m level, which indicates large TKE in the high-speed structures. Usually, the overall average value of TKE at the lower level (50 m) for the entire period is larger than that at the higher level (200 m). Large-scale high-speed structures induce more vigorous turbulence at the lower level. For the selected cases, a clear dependence of the transport efficiency and TKE enhancement factor on the atmospheric conditions, namely, wind speed, wind shear, and *z/L*, are not found.

Finally, we examine the contributions of large-scale high-speed structures from another perspective. For the near-neutral case, Högström (1990) interpreted the results of second-order moment budgets as the effect of "inactive" turbulence. Important evidence for this is the low value (magnitude) of the correlation coefficient between the *u* and *w* velocity components (r_{uw}) in the measurements, a value that becomes lower the more "inactive" turbulence there is in a flow. This is due to the definition,

$$r_{uw} = \frac{\overline{u'w'}}{\sigma_u \sigma_w}, \tag{7}$$

where $\overline{u'w'}$ depends only on the "active" turbulence, while σ_u and σ_w contain both "active" and "inactive" turbulence. For case No. 29, the profiles of the values of r_{uw} in the large-scale high-speed structures as decided above and for the entire analyzed period are shown in Fig. 11. At the lower levels ($\leq$ 100 m), r_{uw} for the entire analyzed period is nearly −0.3, which agrees with the value presented by Högström (1990) for the near-neutral surface layer. On the other hand, the lower values approaching −0.2 are obtained at higher levels. According to the suggestion of Högström (1990), "inactive" turbulence is likely to occur more often at the higher levels than at the lower levels. In fact, the variation with height is due to the decrease of momentum transfer ($-\overline{u'w'}$) towards the higher levels (Fig. 7). In the large-scale high-speed structures, a value close to −0.3 is obtained for all levels. The difference in r_{uw} at the higher levels from the value for the entire period is attributed to the enhanced momentum transfer in the structures.

In the other cases, correlation coefficients (r_{uw}) ranging from −0.2 to −0.38 at the 200-m level are evaluated for the entire analyzed period. At this level, the magnitudes of r_{uw} in the large-scale high-speed structures are higher than those for the entire period in 16 cases. For the lower level (50 m), the values of r_{uw} for the entire period range from −0.24 to −0.32, and in the high-speed structures the magnitudes higher than these are obtained in 20 cases. Although the classification into “active” and “inactive” turbulence is conceptual, these results suggest that large-scale high-speed structures behave like the “active” turbulence.

3.3 Vertical Extent of High-Speed Structures

In this section, the vertical extent of large-scale high-speed structures from the higher level towards the lower level is analyzed. First, the two-point space–time correlation of the original *u* velocity components is examined, in which space is taken in the vertical direction between the 200-m and each lower level and a lag is imposed on the time series of data at each level. Figure 12a shows a space–time correlation field for case No. 29, and where an area of high correlation extends towards the lower level and afterwards in time (positive time lag). After the time–space conversion, this implies the correlation pattern tilting towards the downwind direction, with a resemblance to the conditionally-averaged pattern of the *u* component (Fig. 5). Although correlation coefficients are not significantly high for the greater distance, for the 50-m level the maximum value of 0.31 is found at the time lag of 31 s. This shape of the correlation field is similar to previous results (Townsend 1976; Su et al. 2000). The space–time correlation of the original *u* components reflects the average geometry of turbulent eddies; especially, large-scale high-speed structures as in Fig. 5 possibly have an important influence.

Next, for the purpose of evaluating the influence of large-scale high-speed structures on turbulence in the lower layers, space–time correlation between the 200-m and each lower level is examined for the wavelet coefficients applied to the *u* velocity component.

We use the wavelet coefficients with a large time scale (180 s for case No. 29) for extracting the large-scale structures, as in the above analysis. Figure 12b indicates the space–time correlation field due to large-scale structures for case No. 29. As in the analysis for the original *u* components, the area of high correlation extends to the lower level and tilts towards the downwind direction. Correlation coefficients are larger than those for the original *u* components, and for the 50-m level, the maximum value is 0.67 at a time lag of 16 s. This large value is attributable to the downward extent of large-scale structures from the higher level (200 m in this analysis).

The same evaluation of velocity correlation is made for the other observational cases. Table 2 shows the maximum values of the correlation coefficient between the 200 and 50-m levels for the original *u* velocity components and for the wavelet coefficients applied to the *u* data. The time scales for the wavelet transform are also shown. In all cases, maximum values of the correlation coefficient for the wavelet coefficients are larger than those for the original *u* components. Structures of large horizontal scale, which are extracted using the wavelet transform with a large time scale, also have a large vertical extent. Furthermore, large fluctuations in the large-scale range (wavelet variance at the selected time scale) at the 200-m level tend to induce a large correlation between the higher (200 m) and lower (50 m) levels. The correlation coefficient of this relation is 0.60. With no use of a threshold value for delineating the structures, the values of correlation in Table 2 show the vertical extent and the possible downward influence of large-scale structures.

4 Concluding Remarks

Based on the analysis of observations from sonic anemometers on a meteorological tower, we have investigated the features of large-scale turbulence structures in the near-neutral ABL and their effects on the momentum transfer and the intensity of turbulence. In a typical observational case, wavelet variance spectra for the streamwise velocity

component (u) indicate clear maxima in the large-scale range (100−300 s in this study) at the higher levels (100–200 m). Detecting the events using the wavelet transform with a time scale of 180 s from the time series of u at the highest level (200 m) reveals a descending high-speed structure with a time scale of approximately 100 s (spatial scale of 1 km at the 200-m height). This structure can be thought of as similar to that revealed by Horiguchi et al. (2010) from sodar observations. Moreover, this structure is essentially a specific type of coherent structure that has been previously revealed in experiments on turbulent boundary-layer flows.

Although large-scale high-speed structures can always be observed in the near-neutral ABL, their relative intensity (wavelet variance) varies greatly among the cases. Corresponding to the large spectral values of the wavelet variance in the large-scale range, the region of the –1 power law in the low frequency range of the u spectrum is likely to be related to the emergence of large-scale structures. The relationship between the region of the –1 power law and near-surface organized eddies has already been explored through theoretical considerations (Hunt and Carlotti 2001) and large-eddy simulation (LES) (Foster et al. 2006). Carlotti (2002) showed that the region of the –1 power law can be found in LES and this corresponds to streaky structures. Our study is consistent with earlier work; even so, favourable conditions for the occurrence and development of large-scale high-speed structures could not be examined. For the near-neutral atmospheric surface layer, Katul and Chu (1998) showed that, when strong interaction between the mean flow and turbulent vorticity field occurs, wavelet spectral measurements, and predictions by the analytical solution and dimensional analysis, confirm the existence of the –1 power law in the u spectrum. However, the applicability of this explanation to the u spectrum at higher levels (above the surface layer) is uncertain. The variation of atmospheric conditions during an observational case could have an effect on the turbulence structures in the ABL.

Structures presented in this study are most likely larger than those reported previously in field studies. For example, descending high-speed structures accompanied by ramp

patterns and microfronts in humidity, which were reported by Gao et al. (1989) under near-neutral stability, have a time scale of approximately 20 s above a forest canopy. Large-scale structures in this study have a time scale of approximately 100 s at the level above the surface layer and contain small-scale structures from the inspection of the time series of u. Thus, they are supposed to be related to the "inactive" motions that were discussed by Bradshaw (1967) considering only their scales and positions above the surface. However, large-scale high-speed structures contribute more effectively to momentum transfer, and behave like "active" motions and, moreover, induce more vigorous turbulence in the lower levels. Under strong winds, Mahrt and Howell (1994) also observed large ramp-like structures on horizontal scales of a few km at 45 m above the ground. However, these structures exhibited little correlation with the vertical motion field and were considered "inactive". The different interpretation in our study may be partly attributed to the analytical procedure.

Large-scale high-speed structures observed in this study appear to correspond to "large-scale eddies" (Hunt and Morrison 2000), which exert great influence on inner-layer turbulence. Högström et al. (2002) also explained the neutral surface-layer characteristics in terms of "top-down" mechanisms. They showed that detached eddies, which are brought down from above into the surface layer and are a very effective means for momentum transport, are of eddy-surface-layer height scale (2–4% of the boundary-layer thickness). In contrast, a typical high-speed structure revealed in this study has a large horizontal scale (approximately 1 km at the 200-m height), which is larger than that of the "detached eddies" considered in the previous studies. In spite of the difference in scale, they have a similarity in surface-layer turbulence.

Acknowledgements The authors would like to thank the members of the MRI for the observations using the meteorological tower and a great deal of support for the research.

References

Barthlott C, Drobinski P, Fesquet C, Dubos T, Pietras C (2007) Long-term study of coherent structures in the atmospheric surface layer. Boundary-Layer Meteorol 125:1–24

Bradshaw P (1967) ‘Inactive’ motion and pressure fluctuations in turbulent boundary layers. J Fluid Mech 30:241–258
Carlotti P (2002) Two-point properties of atmospheric turbulence very close to the ground: comparison of a high resolution LES with theoretical models. Boundary-Layer Meteorol 104:381–410
Chen J, Hu F (2003) Coherent structures detected in atmospheric boundary-layer turbulence using wavelet transforms at Huaihe River basin, China. Boundary-Layer Meteorol 107:429–444
Collineau S, Brunet Y (1993) Detection of turbulent coherent motions in a forest canopy part I: wavelet analysis. Boundary-Layer Meteorol 65:357–379
Corino ER, Brodkey RS (1969) A visual investigation of the wall region in turbulent flow. J Fluid Mech 37:1–30
Davenport AG (1961) The spectrum of horizontal gustiness near the ground in high winds. Q J Roy Meteorol Soc 87:194–211
Deardorff JW (1972) Numerical investigation of neutral and unstable planetary boundary layers. J Atmos Sci 29:91–115
Drobinski P, Carlotti P, Newsom RK, Banta RM, Foster RC, Redelsperger J-L (2004) The structure of the near-neutral atmospheric surface layer. J Atmos Sci 61:699–714
Drobinski P, Carlotti P, Redelsperger J-L, Banta RM, Masson V, Newsom RK (2007) Numerical and experimental investigation of the neutral atmospheric surface layer. J Atmos Sci 64:137–156
Foster RC, Vianey F, Drobinski P, Carlotti P (2006) Near-surface coherent structures and the vertical momentum flux in a large-eddy simulation of the neutrally-stratified boundary layer. Boundary-Layer Meteorol 120:229–255
Gao W, Li BL (1993) Wavelet analysis of coherent structures at the atmosphere–forest interface. J Appl Meteorol 32:1717–1725
Gao W, Shaw RH, Paw UKT (1989) Observation of organized structure in turbulent flow within and above a forest canopy. Boundary-Layer Meteorol 47:349–377
Gao W, Shaw RH, Paw UKT (1992) Conditional analysis of temperature and humidity microfronts and ejection/sweep motions within and above a deciduous forest. Boundary-Layer Meteorol 59:35–57
Garratt JR (1992) The atmospheric boundary layer. Cambridge University Press, U.K. 316 pp
Hanafusa T, Fujitani T (1981) Characteristics of high winds observed from a 200 m meteorological tower at Tsukuba Science City. Pap Meteorol Geophys 32:19–35
Hayashi T (1992) Gust and downward momentum transport in the atmospheric surface layer. Boundary-Layer Meteorol 58:33–49
Högström U (1990) Analysis of turbulence structure in the surface layer with a modified similarity formulation for near neutral conditions, J Atmos Sci 47:1949–1972
Högström U, Hunt JCR, Smedman A-S (2002) Theory and measurements for turbulence spectra and variances in the atmospheric neutral surface layer, Boundary-Layer Meteorol 103:101–124
Horiguchi M, Hayashi T, Hashiguchi H, Ito Y, Ueda H (2010) Observations of coherent turbulence structures in the near-neutral atmospheric boundary layer, Boundary-Layer Meteorol 136:25–44
Hunt JCR, Carlotti P (2001) Statistical structure at the wall of the high Reynolds number turbulent boundary layer. Flow Turbul Combust 66:453–475
Hunt JCR, Morrison JF (2000) Eddy structure in turbulent boundary layers. Eur J Mech B 19:673–694
Kaimal JC, Finnigan JJ (1994) Atmospheric boundary layer flows. Oxford University Press, New York, 289 pp
Katul G, Chu C-R (1998) A theoretical and experimental investigation of energy-containing scales in the dynamic sublayer of boundary-layer flows. Boundary-Layer Meteorol 86:279–312
Kline SJ, Reynolds WC, Schraub FA, Runstadler PW (1967) The structure of turbulent boundary layers. J Fluid Mech 30:741–773
Lin C-L, McWilliams JC, Moeng C-H, Sullivan PP (1996) Coherent structures and dynamics in a neutrally stratified planetary boundary layer flow. Phys Fluids 8:2626–2639
Lu C-H, Fitzjarrald DR (1994) Seasonal and diurnal variations of coherent structures over a deciduous forest. Boundary-Layer Meteorol 69:43–69
Mahrt L (1991) Eddy asymmetry in the sheared heated boundary layer. J Atmos Sci 48:472–492
Mahrt L, Howell JF (1994) The influence of coherent structures and microfronts on scaling laws using global and local transforms. J Fluid Mech 260:247–270
Su H-B, Shaw RH, Paw UKT (2000) Two-point correlation analysis of neutrally stratified flow within and above a forest from large-eddy simulation, Boundary-Layer Meteorol 94:423–460

Thomas C, Foken T (2007) Organised motion in a tall spruce canopy: temporal scales, structure spacing and terrain effects. Boundary-Layer Meteorol 122:123–147
Townsend AA (1961) Equilibrium layers and wall turbulence. J Fluid Mech 11:97–120
Townsend AA (1976) The structure of turbulent shear flow. Cambridge University Press, U.K. 429 pp
Wallace JM, Eckelmann H, Brodkey RS (1972) The wall region in turbulent shear flow. J Fluid Mech 54: 39–48
Willmarth WW, Lu SS (1972) Structure of the Reynolds stress near the wall. J Fluid Mech 55: 65–92
Zeng Q-C, Cheng X-L, Hu F, Peng Z (2010) Gustiness and coherent structure of strong winds and their role in dust emission and entrainment. Adv Atmos Sci 27:1–13

Table 1 Mean wind directions (for seven parts) and average values of horizontal wind speed, friction velocity (u_*), and the surface-layer scaling parameter ($|z/L|$) at the 50-m level for the observational cases

Case No.	Date	Time (LST)	Wind direction (°)	Horizontal wind speed (m s^{-1})	u_* (m s^{-1})	$\|z/L\|$
1	3 Dec 1999	0730–1100	297–313	5.9	0.67	0.09
2	3 Dec 1999	1230–1600	295–306	8.6	0.87	0.05
3	7 Dec 1999	1330–1700	285–301	9.4	0.94	0.03
4	12 Dec 1999	1000–1330	306–318	7.8	0.76	0.13
5	26 Dec 1999	1430–1800	296–313	7.3	0.68	0.05
6	4 Jan 2000	1230–1600	282–309	6.3	0.69	0.09
7	11 Jan 2000	1230–1600	287–318	6.4	0.80	0.08
8	20 Jan 2000	1330–1700	275–290	6.0	0.63	0.08
9	20 Jan 2000	1830–2200	288–297	7.1	0.77	0.08
10	21 Jan 2000	1430–1800	293–304	7.9	0.83	0.03
11	31 Jan 2000	1500–1830	317–336	6.9	0.58	0.06
12	9 Feb 2000	0600–0930	294–305	11.1	1.12	0.02
13	10 Feb 2000	0000–0330	260–279	6.5	0.60	0.11
14	10 Feb 2000	0630–1000	268–276	6.9	0.70	0.09
15	16 Feb 2000	1530–1900	308–319	7.6	0.64	0.09
16	21 Feb 2000	1430–1800	295–320	7.9	0.75	0.06
17	22 Feb 2000	1400–1730	294–332	9.1	0.87	0.07
18	29 Feb 2000	0630–1000	262–289	8.2	0.80	0.09
19	29 Feb 2000	1600–1930	300–340	8.7	0.79	0.05
20	9 Mar 2000	1600–1930	326– 1	6.0	0.56	0.06
21	17 Mar 2000	1500–1830	297–303	9.4	0.98	0.04
22	18 Mar 2000	1530–1900	195–205	6.5	0.65	0.11
23	19 Mar 2000	1530–1900	177–187	4.9	0.50	0.07
24	20 Mar 2000	1430–1800	297–309	8.6	0.85	0.09
25	24 Mar 2000	1530–1900	304–320	9.0	0.86	0.05
26	26 Mar 2000	1500–1830	303–316	8.3	0.82	0.05
27	29 Mar 2000	0000–0330	131–143	9.6	0.85	0.05
28	29 Mar 2000	0630–1000	202–219	7.4	0.82	0.08
29	29 Mar 2000	1330–1700	195–207	8.6	0.89	0.06
30	29 Mar 2000	2030–2400	270–314	7.5	0.80	0.06
31	30 Mar 2000	0830–1200	277–310	10.0	0.89	0.14

Table 2 Maximum correlation coefficients between the 200-m and 50-m levels for the original *u* velocity components and for the wavelet coefficients applied to the *u* data

Case No.	Date	Time (LST)	Time scale of the wavelet (s)	Maximum correlation coefficient	
				Original *u*	Wavelet coefficients for *u*
1	3 Dec 1999	0730–1100	244	0.32	0.60
2	3 Dec 1999	1230–1600	184	0.37	0.56
3	7 Dec 1999	1330–1700	156	0.36	0.65
4	12 Dec 1999	1000–1330	236	0.35	0.63
5	26 Dec 1999	1430–1800	232	0.22	0.69
6	4 Jan 2000	1230–1600	252	0.37	0.60
7	11 Jan 2000	1230–1600	236	0.37	0.66
8	20 Jan 2000	1330–1700	156	0.37	0.44
9	20 Jan 2000	1830–2200	164	0.10	0.23
10	21 Jan 2000	1430–1800	240	0.30	0.54
11	31 Jan 2000	1500–1830	108	0.28	0.32
12	9 Feb 2000	0600–0930	124	0.18	0.41
13	10 Feb 2000	0000–0330	172	0.17	0.29
14	10 Feb 2000	0630–1000	180	0.12	0.21
15	16 Feb 2000	1530–1900	188	0.27	0.52
16	21 Feb 2000	1430–1800	140	0.25	0.35
17	22 Feb 2000	1400–1730	112	0.31	0.53
18	29 Feb 2000	0630–1000	180	0.22	0.34
19	29 Feb 2000	1600–1930	164	0.24	0.45
20	9 Mar 2000	1600–1930	220	0.33	0.58
21	17 Mar 2000	1500–1830	112	0.33	0.44
22	18 Mar 2000	1530–1900	124	0.18	0.31
23	19 Mar 2000	1530–1900	172	0.14	0.19
24	20 Mar 2000	1430–1800	260	0.36	0.69
25	24 Mar 2000	1530–1900	196	0.37	0.63
26	26 Mar 2000	1500–1830	192	0.46	0.70
27	29 Mar 2000	0000–0330	140	0.19	0.34
28	29 Mar 2000	0630–1000	172	0.33	0.55
29	29 Mar 2000	1330–1700	180	0.31	0.67
30	29 Mar 2000	2030–2400	156	0.27	0.37
31	30 Mar 2000	0830–1200	240	0.36	0.78

The time scales for the wavelet transform are also shown

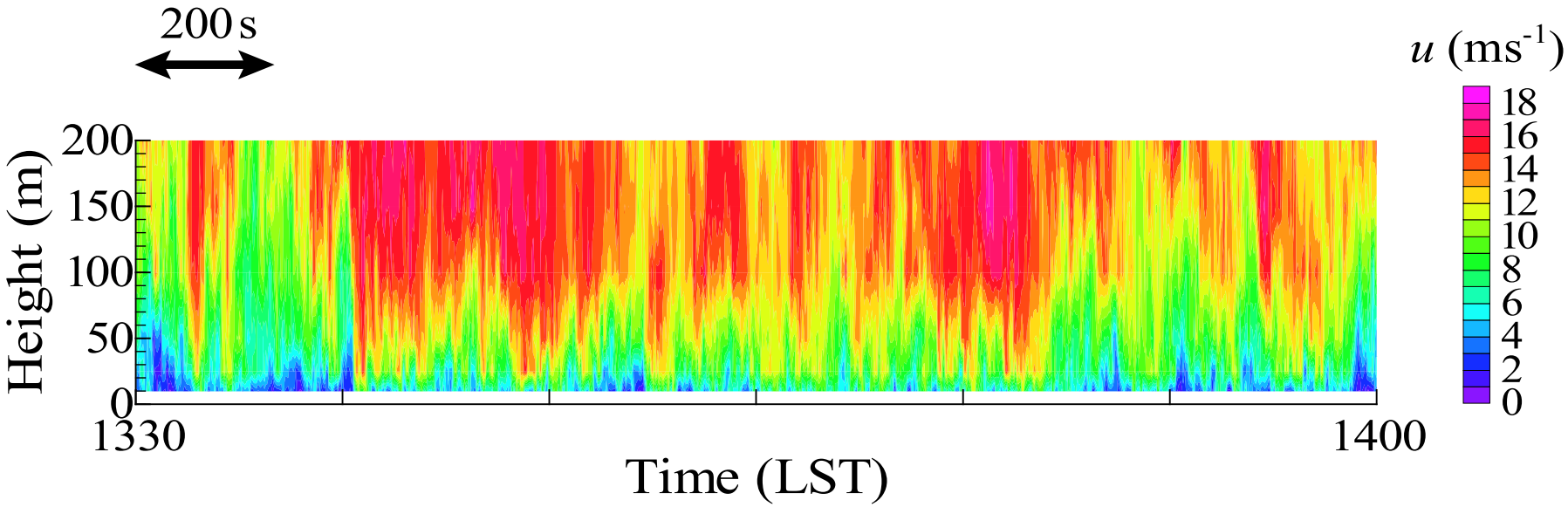

Fig. 1 Time–height cross-section of the *u* velocity component for part 1 of case No. 29 (1330–1700 LST on March 29, 2000). The arrow denotes a time scale of 200 s

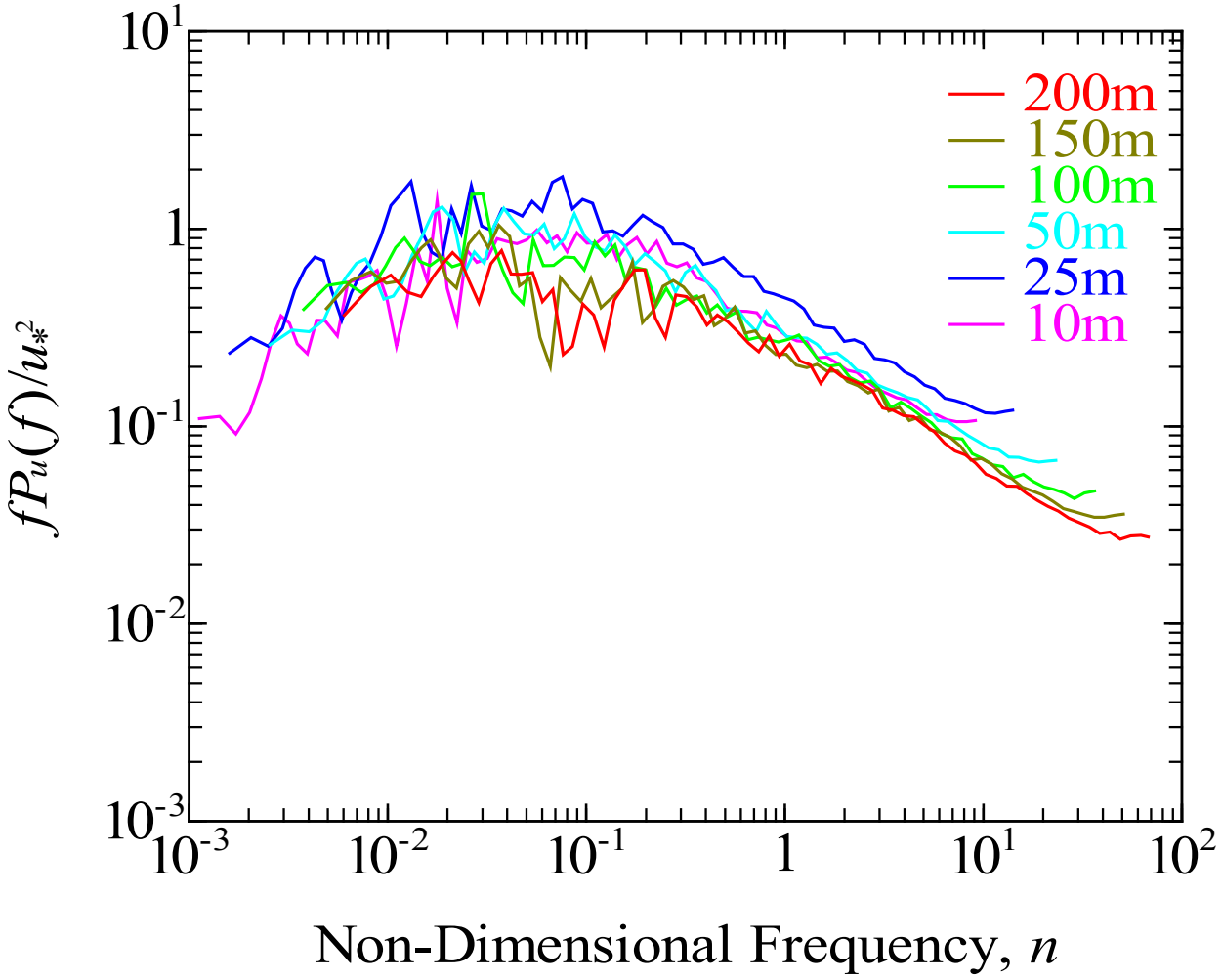

Fig. 2 Normalized power spectra for the *u* velocity component at each level, being averaged over parts 1–7 of case No. 29

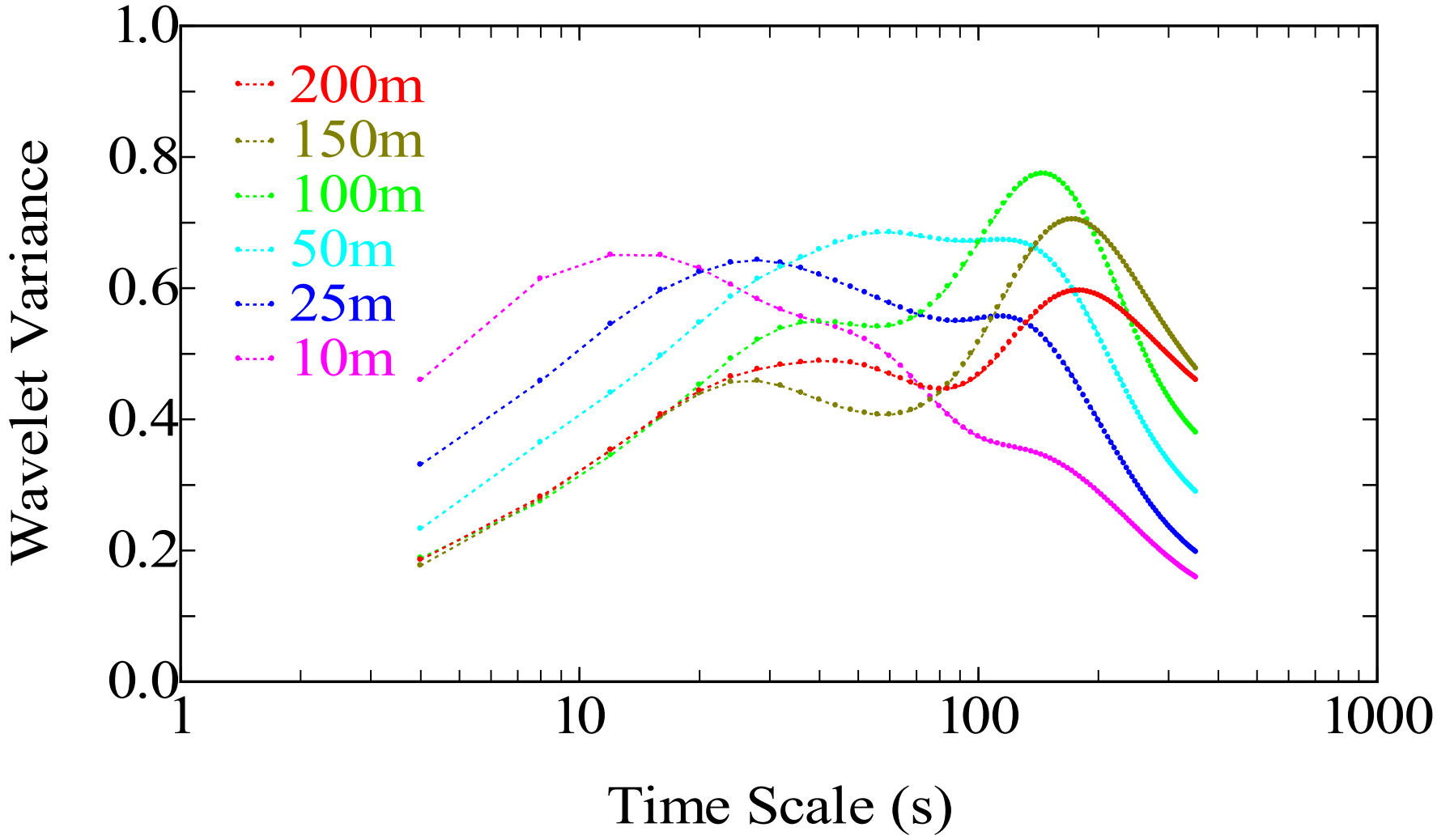

Fig. 3 Wavelet variance spectra for the *u* velocity component as a function of the time scale (case No. 29)

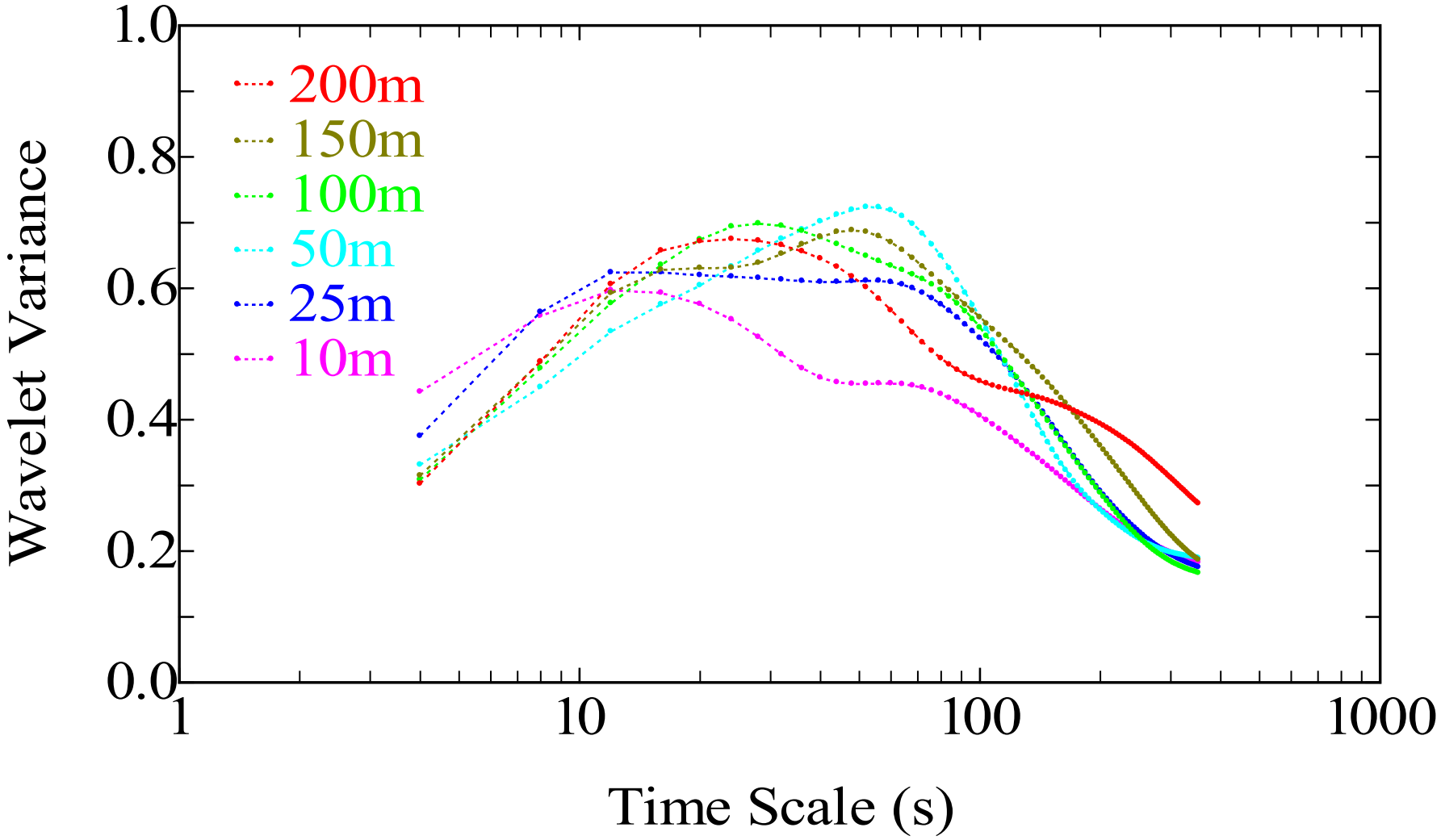

Fig. 4 As Fig. 3, but for the case during 0000–0330 LST on March 29, 2000 (case No. 27)

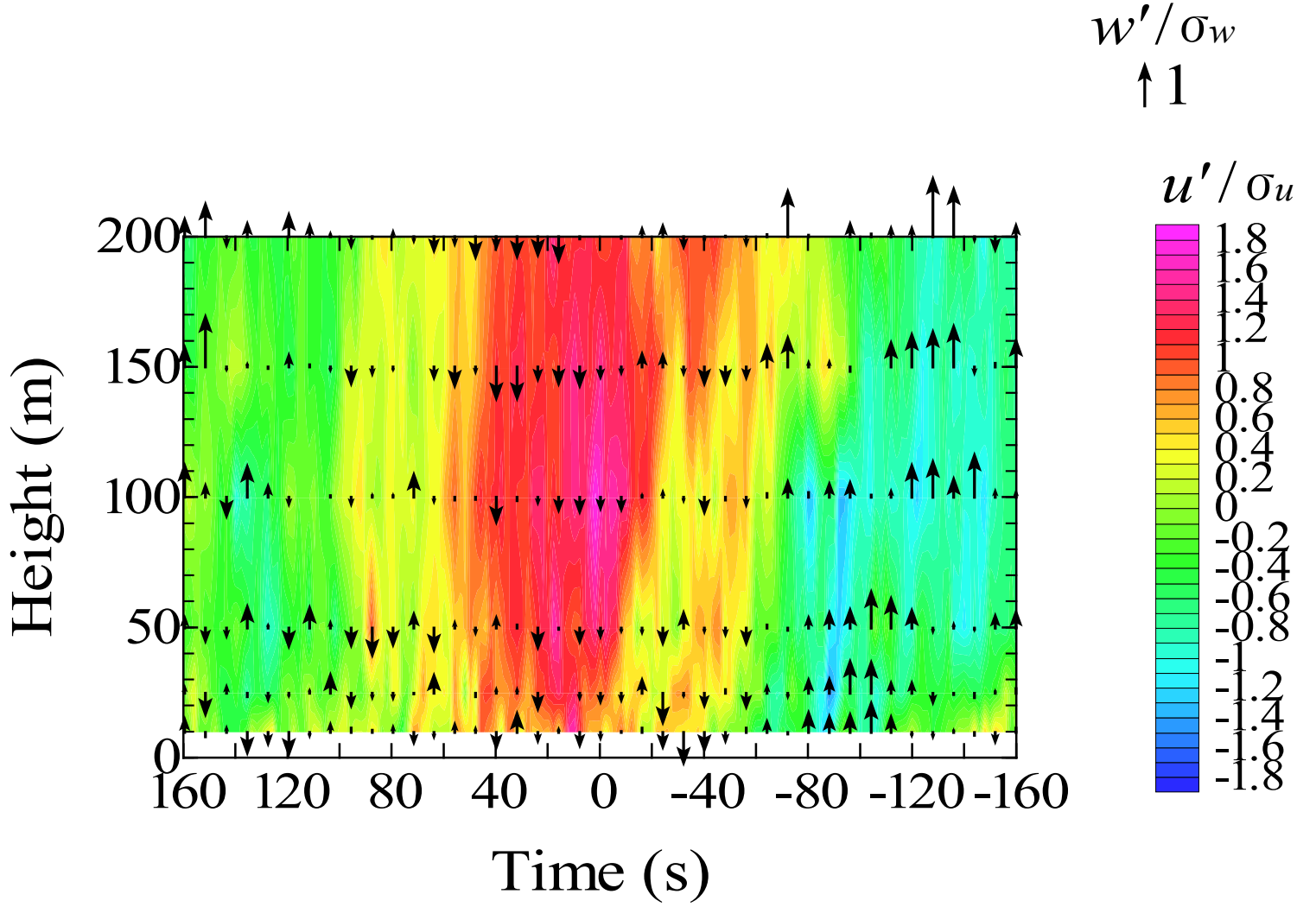

Fig. 5 Conditionally-averaged wind pattern on a time–height cross-section (zero corresponds to the time of the events) for case No. 29. Contours indicate the normalized u' values and arrows denote the normalized w' values

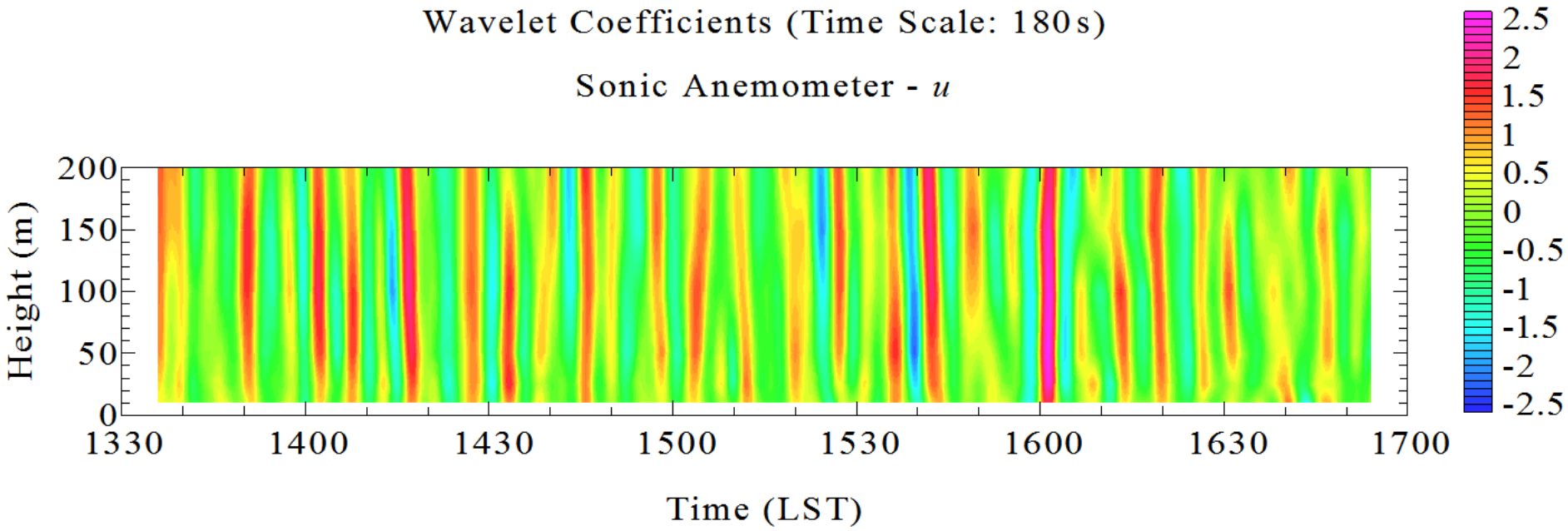

Fig. 6 Time–height cross-section of wavelet coefficients for the *u* velocity component (case No. 29). The time scale for the wavelet transform is 180 s

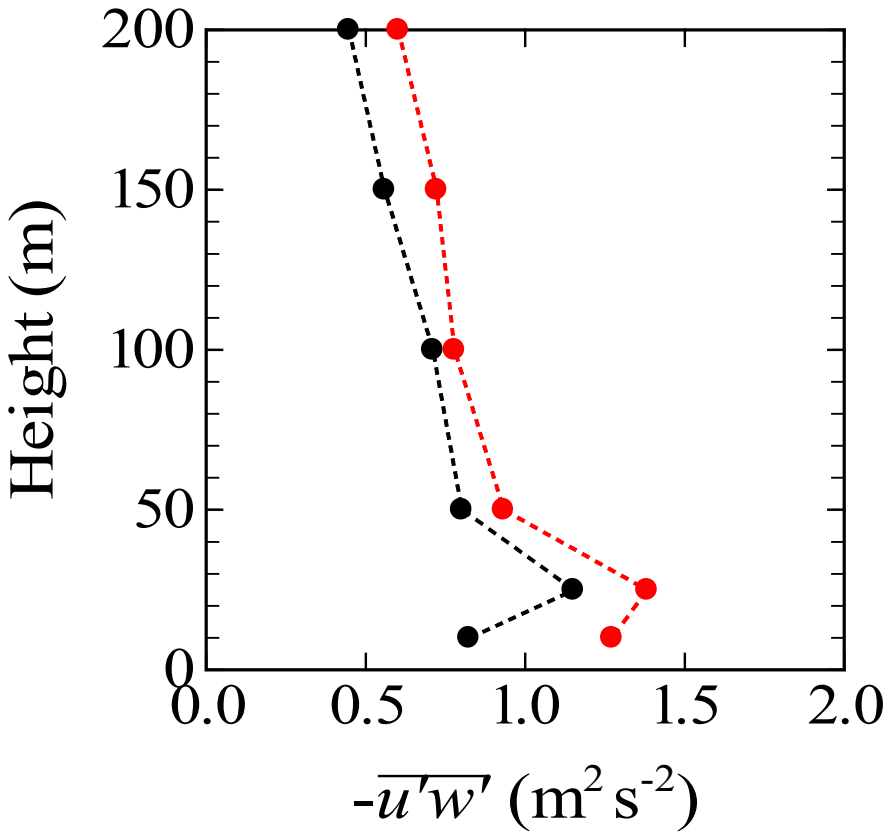

Fig. 7 Average values of $u'w'$ in the large-scale high-speed structures (symbols in red colour) in comparison with the overall average values for the entire analyzed period (in black colour) (case No. 29)

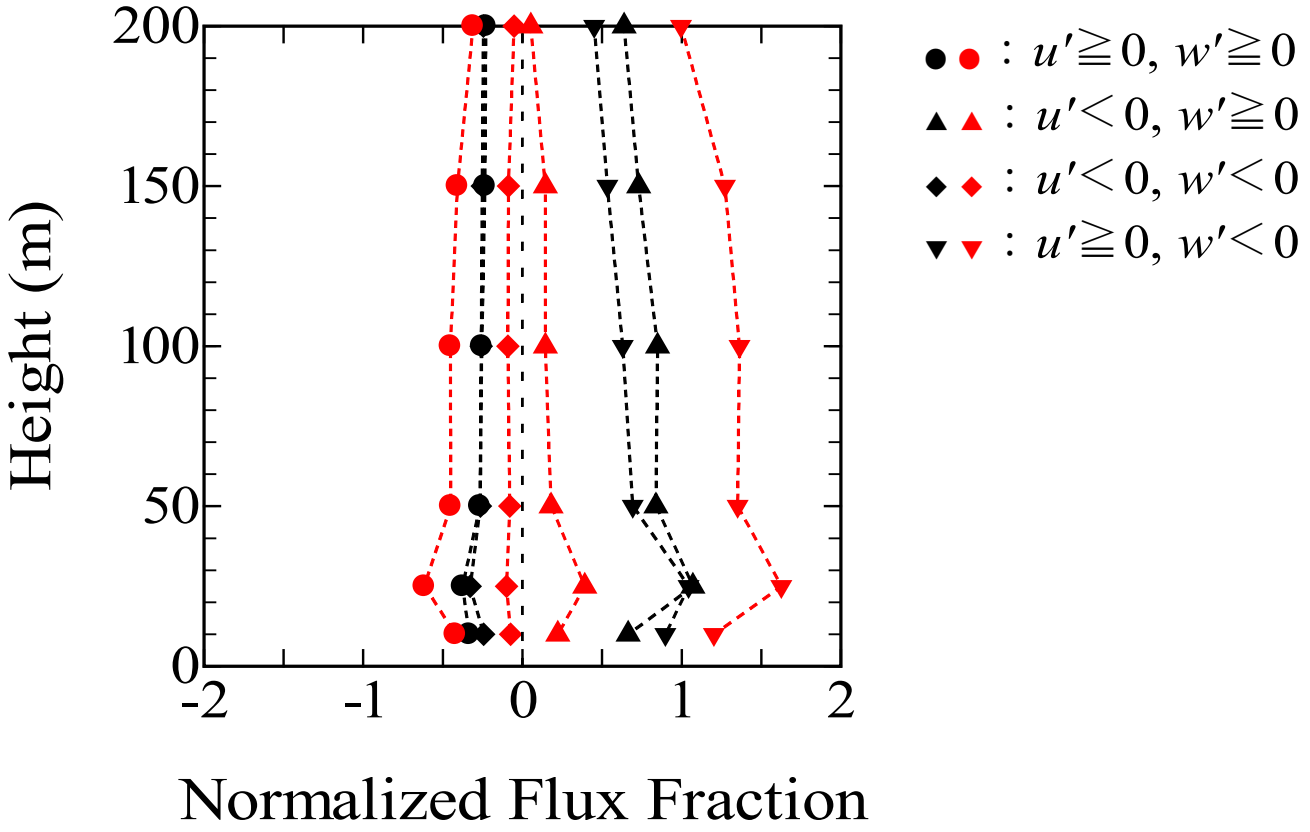

Fig. 8 Normalized flux fractions in the large-scale high-speed structures (symbols in red colour) in comparison with the flux fractions for the entire analyzed period (in black colour) (case No. 29)

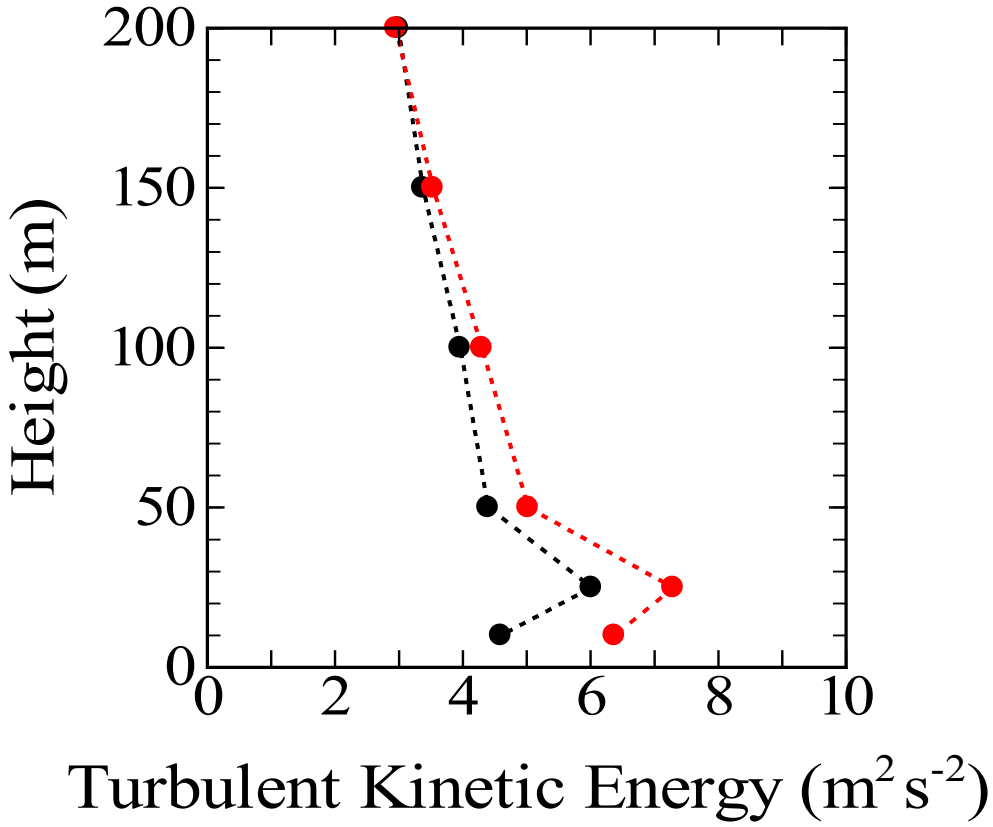

Fig. 9 Average values of instantaneous *e* in the large-scale high-speed structures (symbols in red colour) in comparison with the overall average values (TKE) for the entire analyzed period (in black colour) (case No. 29)

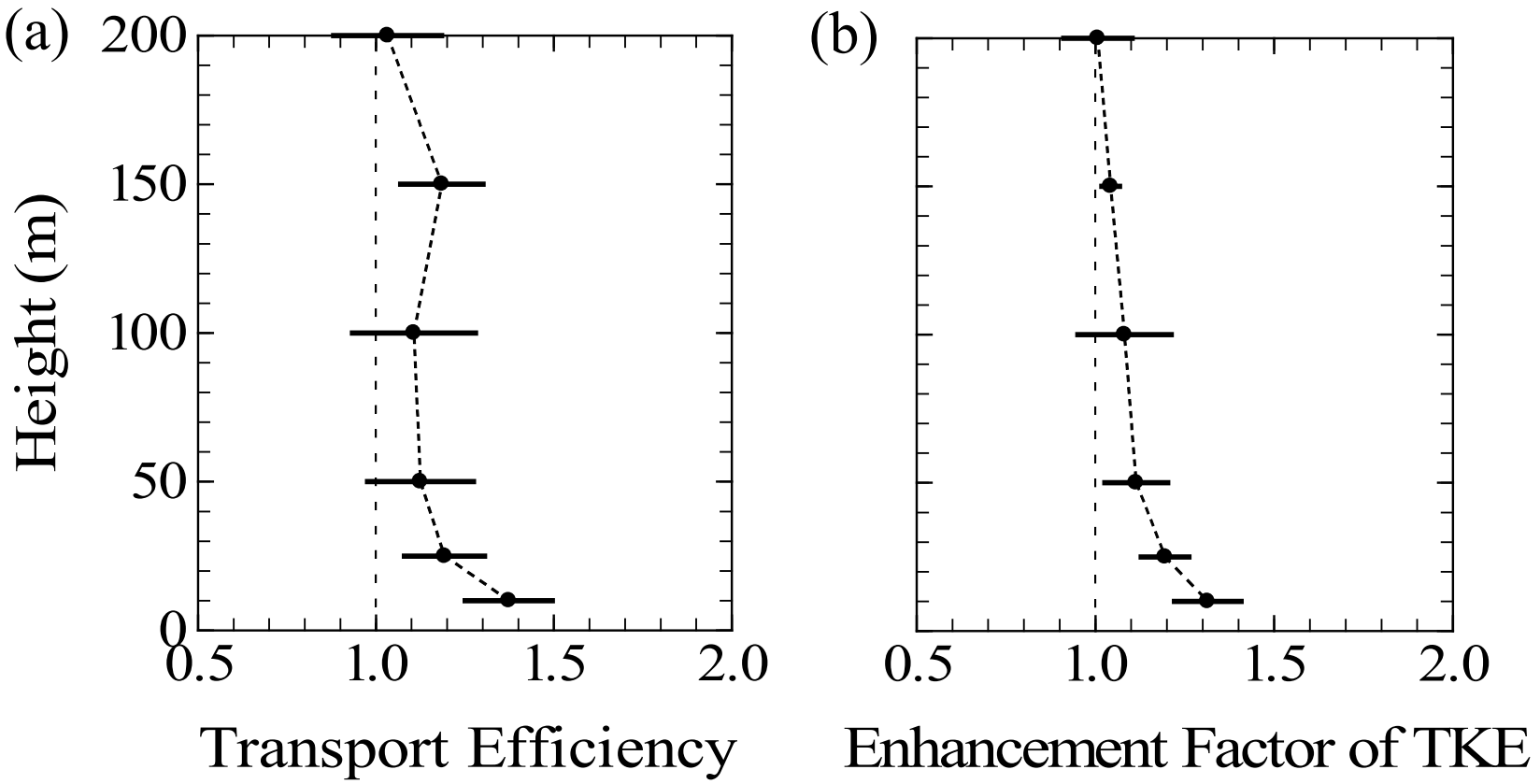

Fig. 10 Transport efficiencies and enhancement factors of TKE by the large-scale high-speed structures. Horizontal bars denote the standard deviations from the mean values for all cases. The number of available cases is limited for the 150 m level

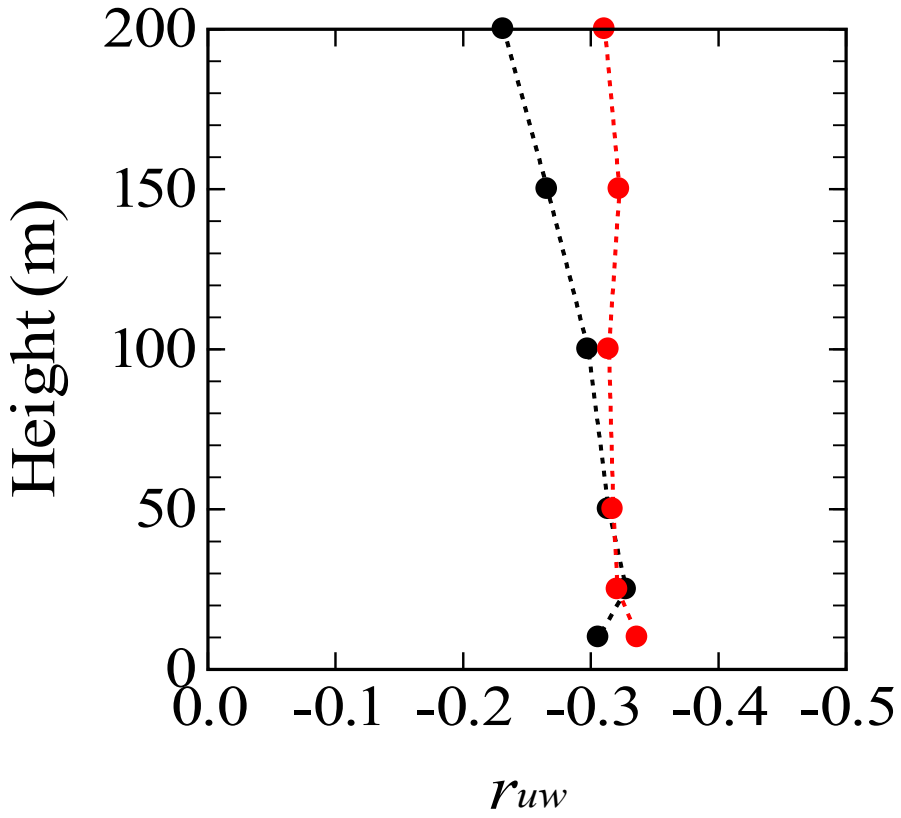

Fig. 11 Correlation coefficients between *u* and *w* velocity components (r_{uw}) in the large-scale high-speed structures (symbols in red colour) in comparison with the coefficients for the entire analyzed period (in black colour) (case No. 29)

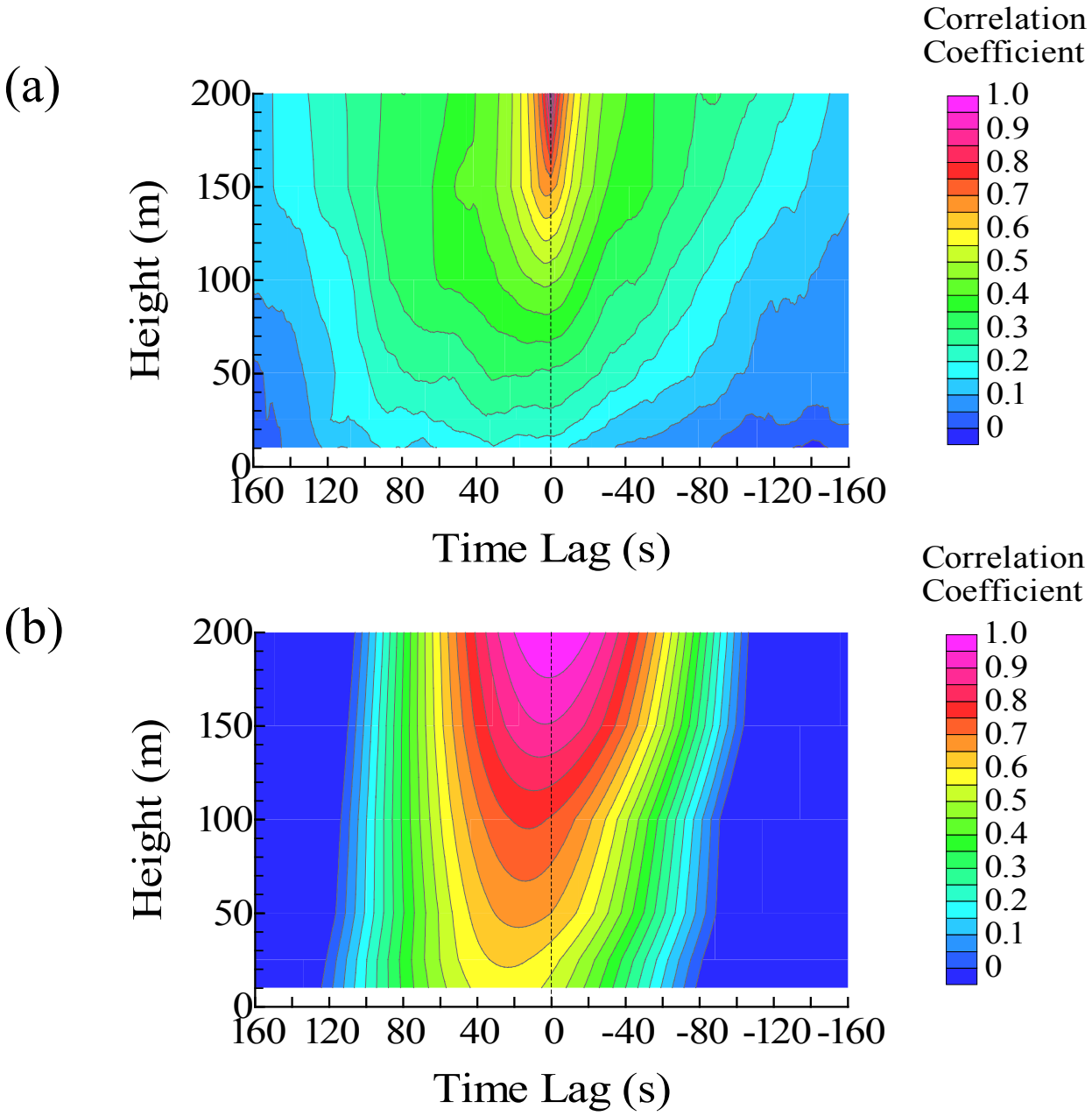

Fig. 12 Two-point space–time correlation of the original *u* velocity components (a) and that of the wavelet coefficients applied to the *u* velocity component (b) (case No. 29). Contours are depicted only in the area of positive correlation